





Phonon-induced near-field resonances in multiferroic BiFeO₃ thin films at infrared and THz wavelengths

Cite as: Appl. Phys. Lett. **116**, 071103 (2020); <https://doi.org/10.1063/1.5133116>

Submitted: 23 October 2019 . Accepted: 01 February 2020 . Published Online: 19 February 2020

Lukas Wehmeier , Tobias Nörenberg, Thales V. A. G. de Oliveira , J. Michael Klopff, Seung-Yeul Yang, Lane W. Martin , Ramamoorthy Ramesh, Lukas M. Eng , and Susanne C. Kehr



View Online



Export Citation



CrossMark



Measure Ready
M91 FastHall™ Controller

A revolutionary new instrument
for complete Hall analysis

See the video 

Lake Shore
CRYOTRONICS

Phonon-induced near-field resonances in multiferroic BiFeO₃ thin films at infrared and THz wavelengths

Cite as: Appl. Phys. Lett. **116**, 071103 (2020); doi: [10.1063/1.5133116](https://doi.org/10.1063/1.5133116)

Submitted: 23 October 2019 · Accepted: 1 February 2020 ·

Published Online: 19 February 2020



View Online



Export Citation



CrossMark

Lukas Wehmeier,^{1,a)} Tobias Nörenberg,¹ Thales V. A. C. de Oliveira,^{1,2} J. Michael Klopff,² Seung-Yeul Yang,³ Lane W. Martin,⁴ Ramamoorthy Ramesh,⁴ Lukas M. Eng,^{1,5} and Susanne C. Kehr^{1,b)}

AFFILIATIONS

¹Institute of Applied Physics, Technische Universität Dresden, 01062 Dresden, Germany

²Institute of Radiation Physics, Helmholtz-Zentrum Dresden-Rossendorf, 01328 Dresden, Germany

³SanDisk, Western Digital Technologies Inc., Milpitas, California 95035, USA

⁴Department of Materials Science and Engineering, University of California, Berkeley, California 94720, USA

⁵ct.qmat, Dresden-Würzburg Cluster of Excellence-EXC 2147, Technische Universität Dresden, 01062 Dresden, Germany

^{a)}Electronic mail: lukas.wehmeier@tu-dresden.de

^{b)}Electronic mail: susanne.kehr@tu-dresden.de

ABSTRACT

Multiferroic BiFeO₃ (BFO) shows several phonon modes at infrared (IR) to THz energies, which are expected to carry information on any sample property coupled to crystal lattice vibrations. While macroscopic IR studies of BFO are often limited by single-crystal size, scattering-type scanning near-field optical microscopy (s-SNOM) allows for IR thin film spectroscopy of nanoscopic probing volumes with negligible direct substrate contribution to the optical signal. In fact, polaritons such as phonon polaritons of BFO introduce a resonant tip-sample coupling in s-SNOM, leading to both stronger signals and enhanced sensitivity to local material properties. Here, we explore the near-field response of BFO thin films at three consecutive resonances (centered around 5 THz, 13 THz, and 16 THz), by combining s-SNOM with a free-electron laser. We study the dependence of these near-field resonances on both the wavelength and tip-sample distance. Enabled by the broad spectral range of the measurement, we probe phonon modes connected to the predominant motion of either the bismuth or oxygen ions. Therefore, we propose s-SNOM at multiple near-field resonances as a versatile and very sensitive tool for the simultaneous investigation of various sample properties.

Published under license by AIP Publishing. <https://doi.org/10.1063/1.5133116>

Bismuth ferrite, BiFeO₃ (BFO), is a perovskite of the highest scientific and technological interest,¹ which shows many fascinating properties such as ferroelectric and antiferromagnetic—i.e., multiferroic—responses,^{1,2} conductive domain walls,³ and anomalous photovoltaic effects.⁴ Interesting applications are proposed for multiferroic memory devices and spintronics¹ and as the base material for energy storage devices.⁵

For deeper understanding of the multiferroic nature of BFO, detailed knowledge on the various excitations that occur at low energies—i.e., at infrared (IR) to THz wavelengths—such as phonons, magnons, spin excitations, and combinations thereof is essential. Following scientific interest in BFO, these excitations have been probed with a manifold of techniques, e.g., Raman and IR spectroscopy, time-domain terahertz spectroscopy, and neutron scattering.⁶

Among these methods, IR spectroscopy may be considered one of the most direct methods to probe IR active phonon modes. It has been applied to ceramic BFO samples,^{6–9} bulk single crystals,^{10,11} and thin film samples at cryogenic temperatures.⁶ However, the phonon information obtainable via standard IR spectroscopy suffers from severe drawbacks: ceramic samples generally show lower crystal quality than bulk samples and yield averaged phonon properties because of their polycrystalline nature.^{6–9} Due to the relatively large probing volume of (far-field) IR spectroscopy, available bulk crystals are usually too small for fully polarization-dependent measurements at larger wavelengths/lower energies.^{6,10,11} Therefore, while on bulk samples the E-symmetry phonon modes could be completely characterized (spectral position, oscillator strength, and damping),^{10,11} for the (also IR-active) A₁ phonon modes, only the spectral position could be assigned.¹⁰ For IR

spectroscopy on thin film samples, the large probing volume causes the sensitivity of the method to depend on optical properties of the substrate.⁶

Near-field spectroscopy and scattering-type scanning near-field optical microscopy (s-SNOM) combine the material specificity of optical and IR techniques with the wavelength-independent^{12,13} nanoscale resolution of atomic force microscopy,^{14–17} making s-SNOM an outstanding tool for investigations down to the THz region.^{13,17–22} In addition to the spatial resolution, the probing depth of s-SNOM of about 100 nm^{21,23–26} presents a major advantage for the investigation of small volumes or thin film samples, allowing for IR thin film spectroscopy with negligible direct substrate contribution to the optical signal.²⁷

The signal strength of s-SNOM is greatly enhanced via polariton-induced resonant tip-sample interaction,^{12,17,27,30–32,34–45} which is of special advantage when exploring technically challenging wavelength regimes,^{17,45} such as the “THz gap” (30–300 μm , i.e., 1–10 THz).⁴⁶ Particularly, sample-resonant s-SNOM provides enhanced sensitivity to the smallest material variations such as doping level and charge carrier concentration,^{22,36,39,47} optical anisotropy tensor orientation in

ferroelectric materials,^{30,31,40,48} polymorphism,³⁶ and local stress distribution.³⁷ Crystalline materials support several excitation modes, making broad-wavelength observation of multiple characteristic material resonances in a single material most desirable.⁴²

Here, we investigate three consecutive phonon-polariton-induced near-field resonances in BFO with respect to both the spectral position and the dependence on tip-sample distance h . The smallest-wavelength near-field resonance of BFO at $\approx 18 \mu\text{m}$ (16.7 THz) was partly investigated in the context of BFO-based superlenses;⁴⁹ the longest-wavelength resonance investigated is found at $\approx 60 \mu\text{m}$ (5.0 THz), i.e., within the THz gap.

We examine two epitaxially grown BFO thin-film samples on the (001) SrTiO₃ substrate: For our measurements at wavelengths $\lambda \lesssim 18 \mu\text{m}$, we use a thin film of 200 nm thickness grown by pulsed laser deposition and at $\lambda > 18 \mu\text{m}$ we study a film of 1050 nm thickness grown by chemical vapor deposition. Different film thicknesses were used due to sample availability. Employing the literature E-symmetry phonon data and suitable formula given by Lobo *et al.*,¹⁰ we calculate the permittivity $\epsilon = \epsilon' + i\epsilon''$ of BFO in the wavelength range from 5 to 70 μm [Fig. 1(a)].⁵⁰ For the displayed permittivity, we

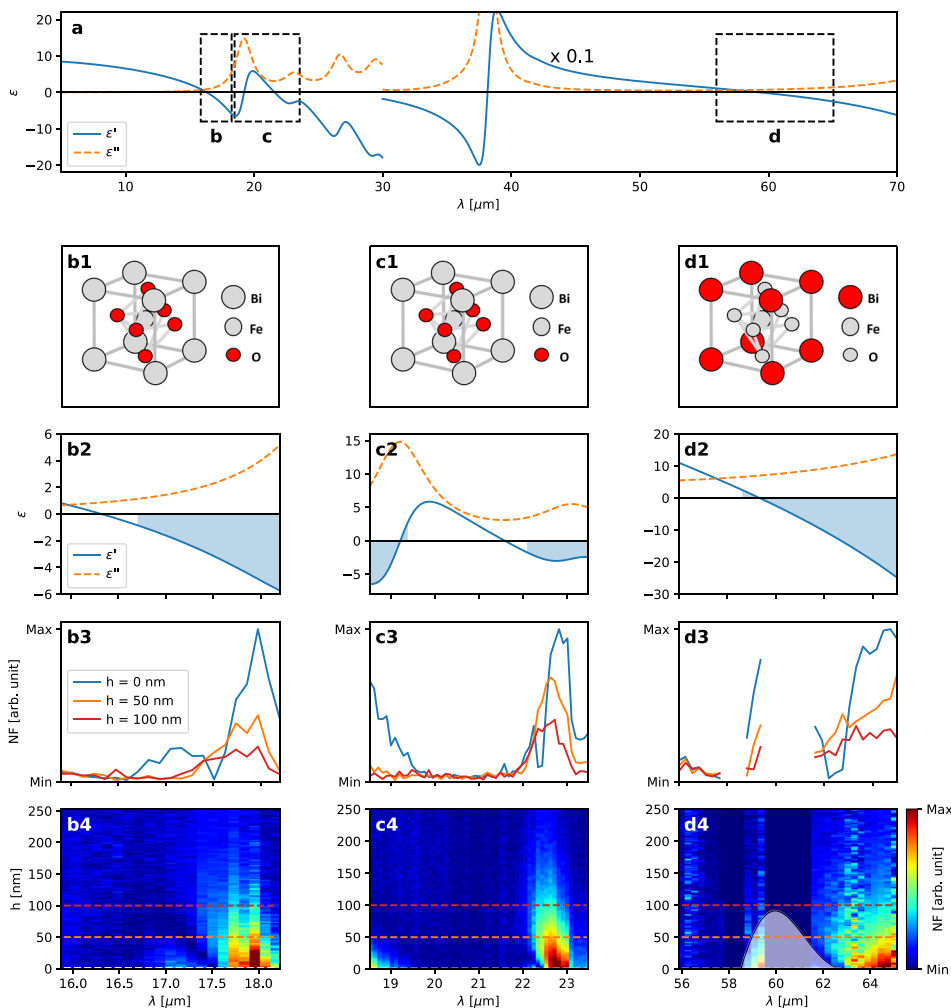


FIG. 1. In the IR wavelength range from $5 \mu\text{m} \leq \lambda \leq 70 \mu\text{m}$, BFO shows three regions with $\epsilon' < 0$, enabling resonant near-field enhancement. (a) Overview of the permittivity $\epsilon = \epsilon' + i\epsilon''$ of BFO calculated from literature data.¹⁰ For better visibility, ϵ is multiplied with a factor of 0.1 for $\lambda > 30 \mu\text{m}$. We distinguish three interesting regions where ϵ' changes the sign from positive to negative, which are marked with boxes; enlarged views are displayed in (b2), (c2), and (d2), respectively. In these regions, the phonon modes are dominated by either the motion of the oxygen or bismuth ions:^{10,28} (b1), (c1), and (d1) show a sketch of the respective ion position within the BFO unit cell.⁵⁷ As predicted (refer to the main text), in the three selected wavelength regions, an enhanced near-field response (NF) is observed. Corresponding to the wavelength range of (b2), (c2), and (d2), respectively, (b3), (c3), and (d3) each display three near-field spectra taken at tip-sample distances $h = 0 \text{ nm}$, 50 nm, and 100 nm. Wavelength regions of the enhanced near-field response are shaded in (b2), (c2), and (d2). (b4), (c4), and (d4) show the spectral near-field response for tip-sample distances $0 \text{ nm} \leq h \leq 250 \text{ nm}$, with the h -positions of (b3), (c3), and (d3) marked by horizontal lines. A characteristic blueshift of the enhanced near-field response with increasing h ^{27,29–33} is clearly observable, leading to a typically lobe-like feature in the false color plots.^{27,30,31,33} As a guide to the eye, in (d4), the approximate position of the first lobe is marked with a white shaded area.

calculate the expected near-field response using the dipole model^{52,53} (see the [supplementary material](#)). As a rule of thumb for sufficiently low absorption, a near-field resonance may be observed whenever the real part of a material's permittivity ϵ' falls in the range of $-10 \leq \epsilon'_{\text{res}} \leq -1$, with ϵ'_{res} depending on the imaginary part of the permittivity ϵ'' .^{12,27,35} In the calculated wavelength region, BFO shows three spectral positions that fulfill this condition [marked with boxes in Fig. 1(a) and enlarged in Figs. 1(b2), 1(c2), and 1(d2), respectively]. Note that close to an absorption maximum (i.e., for large ϵ''), no observable near-field resonance is expected due to pronounced damping, even for suitable ϵ' . Calculations also predict that the spectral position of a near-field resonance must blue shift with the increased tip-sample distance,^{29,51} which has been experimentally confirmed for mid-IR wavelengths,^{27,29–33} but so far it has not been explored at larger wavelengths.

The wavelength regions of interest are investigated with a home-built s-SNOM that implements demodulation at higher harmonics of the mechanical cantilever oscillation frequency^{53,54} and a self-homodyne detection scheme, with the latter leading to a combined response of near-field amplitude and phase.^{17,53} For illumination, we use the tunable narrow-band free-electron laser (FEL) at the Helmholtz-Zentrum Dresden-Rossendorf (HZDR), Germany,^{27,31,40,41,55} which is a linearly-polarized, pulsed laser source at 13 MHz repetition rate covering the wavelength range of 5–250 μm , i.e., 1.2–60.0 THz.⁵⁶ The experimental setup is described in detail elsewhere.^{13,27} For detection at mid-IR wavelengths, we use liquid-nitrogen-cooled mercury cadmium telluride (MCT) detectors having different cut-off wavelengths. In the THz range, we utilize a liquid-helium-cooled gallium-doped germanium (Ge:Ga) photoconductor, while the experiment is performed in a nitrogen-purged environment. The near-field response is normalized to the incident power and the corresponding detector response and has been investigated with respect to both tip-sample distance h and incident wavelength λ .

The measured near-field spectra (second-harmonic demodulation and p-polarized incident light) are displayed in Figs. 1(b3)–1(d4), with wavelength ranges matching to the permittivity ϵ in Figs. 1(b2), 1(c2), and 1(d2), respectively. Figs. 1(b3), 1(c3), and 1(d3) each display near-field spectra recorded at the three different tip-sample distances $h = 0$ nm, 50 nm, and 100 nm. Figs. 1(b4), 1(c4), and 1(d4) present false-color plots of spectra for $0 \text{ nm} \leq h \leq 250$ nm. As expected, an enhanced near-field response is observed in all three wavelength regions, as discussed in the following. Note that the permittivity data displayed in Figs. 1(b2), 1(c2), and 1(d2) may be used for qualitative comparison only, as it is derived from literature data for a single polarization direction,¹⁰ and sample properties may vary, e.g., due to substrate effects and different growth conditions.^{7,10}

The near-field resonance at the smallest wavelengths [Figs. 1(b3) and 1(b4)] is induced by phonon modes dominated by the collective motion of the oxygen ions.^{10,28} Figure 1(b1) displays their position within the BFO unit cell. The enhanced near-field signal starts at $\lambda_{\text{res},1} \geq 16.7 \mu\text{m}$ (18.0 THz) and shows two local maxima at $\lambda \approx 17.2 \mu\text{m}$ (17.4 THz) and $\approx 17.9 \mu\text{m}$ (16.8 THz). Note that the self-homodyne detection scheme may introduce additional maxima/minima not present when using other detection schemes.²⁷

Similar to the first resonance, the second near-field resonance is connected to oxygen motion [Fig. 1(c1)].^{10,28} It also shows two local maxima and is observed for $\lambda_{\text{res},2} \geq 22.1 \mu\text{m}$ (13.6 THz) [Figs. 1(c3)

and 1(c4)], which corresponds to a width of $\geq 1.4 \mu\text{m}$. While the second resonance continues beyond the large-wavelength end in Figs. 1(c2)–1(c4), the wavelength range is sufficiently large to show the first near-field resonance continuing to $\lambda_{\text{res},1} \leq 19.4 \mu\text{m}$ (15.5 THz). Assuming similar material properties for the 200 nm-thick and 1050 nm-thick films, this yields a total width of the first near-field resonance of approximately 2.7 μm .

Different from the first two resonances, the third resonance [Figs. 1(d3) and 1(d4)] is related to phonons dominated by the motion of the bismuth ions [Fig. 1(d1)].^{10,28} An enhanced near-field response occurs at $\lambda_{\text{res},3} \geq 58.6 \mu\text{m}$ (5.1 THz) and continues throughout the wavelength range of the measurement, i.e., up to 65.0 μm (4.6 THz), resulting in a width of $\geq 6.4 \mu\text{m}$. Similar to the other resonances, two local maxima can be observed. Here, the first local maximum [approximate position marked with a white shaded area in Fig. 1(d4)] could be measured partly only, as certain wavelengths exist at which the FEL was not lasing for the used undulator and cavity settings. In Figs. 1(d3) and 1(d4), this applies to the two wavelength ranges from approximately 57.8 to 58.7 μm and 59.5 to 61.5 μm .

A summary of the wavelength ranges and spectral widths of all measured resonances is listed in Table I. All investigated resonances confirm the expected, characteristic blueshift with increasing tip-sample distance h ,^{27,29–33} which results in a typical lobe-like shape in the false-color plots [Figs. 1(b4), 1(c4), and 1(d4)].^{27,30,31,33} A similar behavior of the resonances suggests that at larger wavelengths the interaction mechanism between the probe and the sample is the same as for lower wavelengths, as expected. Yet, it is an important observation that resonant near-field examination provides well-observable signals over the whole mid-IR and even the far-IR/THz regime.

Comparing the observed near-field resonances with the permittivity data derived from the literature,¹⁰ we find the following: for the two modes that are dominated by oxygen motion, the corresponding resonances [Figs. 1(b3), 1(b4), 1(c3), and 1(c4)] match well to the macroscopic data, showing enhanced near-field signals for $-6 \leq \epsilon'_{\text{res}} \leq -1$. For the third resonance [Figs. 1(d3) and 1(d4)], the agreement of the spectral position with the expectation derived from the permittivity [Fig. 1(d2)] is less accurate. Particularly, a significant enhancement of the near-field signal is observed for wavelengths as small as 58.6 μm , for which the literature assumes permittivity values of $\epsilon = 2.6 + 6.6i$. Hence, no resonant enhancement is expected, albeit the resonance will be broadened due to the larger imaginary part ϵ'' compared to the resonances at smaller wavelengths (see the [supplementary material](#)). The mismatch may partly be explained by different growth conditions of our sample in comparison to literature data. However, we assume that the polarization of the probing field plays the major role in this spectral mismatch: The literature data were obtained for phonon modes with E symmetry, i.e., corresponding to

TABLE I. Wavelength λ , frequency ν , and spectral width Δ_λ of the BFO near-field resonances investigated.

No.	λ_{start} (μm)	ν_{start} (THz)	λ_{end} (μm)	ν_{end} (THz)	Δ_λ (μm)
1	16.7	18.0	19.4	15.5	2.7
2	22.1	13.6	≥ 23.5	≤ 12.8	≥ 1.4
3	58.6	5.1	≥ 65.0	≤ 4.6	≥ 6.4

an optical polarization within the crystallographic ab -plane.¹⁰ On the other hand, s -SNOM is generally sensitive to an average over different polarization directions,^{30,31,48} which here means sensitivity to both E and A_1 phonon modes. Depending on the reference at room temperature, two¹⁰ or even three^{7,8} of the four^{7,8,10,28} A_1 modes are expected within the range spanning from 44 to 76 μm , i.e., at wavelengths close to this near-field resonance, which will, hence, influence the permittivity and thereby the spectral position of the resonance. Notably, the strength of the A_1 modes in BFO increases with the wavelength,⁸ which explains their enhanced significance for the long-wavelength near-field resonances.

The spectral position obtained for BFO resonance at the smallest wavelength agrees very well with near-field resonances previously found around $\lambda_{\text{res}} \approx 18 \mu\text{m}$ on thin films and being reported in the context of BFO-based superlenses.⁴⁹ Here, we also determined the spectral positions of the BFO near-field resonances at larger wavelengths and their dependence on the tip-sample distance. Since different near-field resonances are induced by different polariton modes (here phonon modes) that are related to the motion of different atoms within the crystal, we assume that access to multiple modes will also provide a possibility to optically probe different sample properties, which will be a most intriguing topic for future research. Additionally, different polaritonic resonances may show different near-field decays.³³ Here, our results may help to develop a new technique to distinguish different polariton modes over a very broad wavelength regime.

In conclusion, we investigated three consecutive phonon-induced near-field resonances in BFO from the mid-IR up to the far-IR/THz regime. The small probing volume of s -SNOM allowed for investigating thin film samples with negligible direct substrate influences. For all resonances, i.e., including the so far unexplored resonances at larger wavelengths, we could observe the same characteristic blueshift with increasing tip-sample distance known from mid-IR resonances. For the two near-field resonances attributed to motion of oxygen ions in the crystal, we find an excellent match to macroscopic literature data. Notably, the resonance at the longest wavelength, dominated by bismuth ion motion,²⁸ appears at slightly smaller wavelengths than expected from literature, which we attribute to an additional excitation of A_1 -modes in the crystal. Depending on the wavelength regime, the BFO near-field resonances investigated here are connected to motions either dominated by oxygen or bismuth ions.²⁸ Therefore, we propose using s -SNOM at multiple near-field resonances as a sensitive tool for the simultaneous investigation of different sample properties. Expanding sample-resonant s -SNOM regarding both the investigated wavelength regimes and dependence on the tip-sample distance, our work highlights the potential of this technique for the nanoscale optical material characterization, especially for nanospectroscopic inspection of thin films.

See the [supplementary material](#) for calculations of the expected near-field response using the dipole model.

We are grateful to J. Döring, F. Kuschewski, and D. Lang for assistance with the s -SNOM measurements. Parts of this research were carried out at ELBE at the Helmholtz-Zentrum Dresden-Rossendorf e. V., a member of the Helmholtz Association. We would like to thank P. Michel, S. Winnerl and the FELBE team for

assistance. This project was funded by the DFG under Grant No. KE2068/2-1 and by the BMBF under Grant Nos. 05K16ODA, 05K16ODC, 05K19ODA, and 05K19ODB, as well as by the Würzburg-Dresden Cluster of Excellence on Complexity and Topology in Quantum Matter (ct.qmat) and by the TU Dresden graduate academy.

REFERENCES

- G. Catalan and J. F. Scott, *Adv. Mater.* **21**, 2463 (2009).
- J. Wang, J. B. Neaton, H. Zheng, V. Nagarajan, S. B. Ogale, B. Liu, D. Viehland, V. Vaithyanathan, D. G. Schlom, U. V. Waghmare, N. A. Spaldin, K. M. Rabe, M. Wuttig, and R. Ramesh, *Science* **299**, 1719 (2003).
- J. Seidel, L. W. Martin, Q. He, Q. Zhan, Y.-H. Chu, A. Rother, M. E. Hawkridge, P. Maksymovych, P. Yu, M. Gajek, N. Balke, S. V. Kalinin, S. Gemming, F. Wang, G. Catalan, J. F. Scott, N. A. Spaldin, J. Orenstein, and R. Ramesh, *Nat. Mater.* **8**, 229 (2009).
- S. Y. Yang, J. Seidel, S. J. Byrnes, P. Shafer, C. H. Yang, M. D. Rossell, P. Yu, Y. H. Chu, J. F. Scott, J. W. Ager, L. W. Martin, and R. Ramesh, *Nat. Nanotechnol.* **5**, 143 (2010).
- H. Pan, J. Ma, J. Ma, Q. Zhang, X. Liu, B. Guan, L. Gu, X. Zhang, Y.-J. Zhang, L. Li, Y. Shen, Y.-H. Lin, and C.-W. Nan, *Nat. Commun.* **9**, 1813 (2018).
- S. Skiadopoulou, V. Goian, C. Kadlec, F. Kadlec, X. F. Bai, I. C. Infante, B. Dkhil, C. Adamo, D. G. Schlom, and S. Kamba, *Phys. Rev. B* **91**, 174108 (2015).
- S. Kamba, D. Nuzhnyy, M. Savinov, J. Šebek, J. Petzelt, J. Prokleska, R. Haumont, and J. Kreisel, *Phys. Rev. B* **75**, 024403 (2007).
- G. A. Komandin, V. I. Torgashev, A. A. Volkov, O. E. Porodinkov, I. E. Spektor, and A. A. Bush, *Phys. Solid State* **52**, 734 (2010).
- N. E. Massa, L. del Campo, D. de Souza Meneses, P. Echegut, G. F. L. Fabbris, G. D. M. Azevedo, M. J. Martínez-Lope, and J. A. Alonso, *J. Appl. Phys.* **108**, 084114 (2010).
- R. P. S. M. Lobo, R. L. Moreira, D. Lebeugle, and D. Colson, *Phys. Rev. B* **76**, 172105 (2007).
- J. Lu, M. Schmidt, P. Lunkenheimer, A. Pimenov, A. A. Mukhin, V. D. Travkin, and A. Loidl, *J. Phys. Conf. Ser.* **200**, 012106 (2010).
- T. Taubner, R. Hillenbrand, and F. Keilmann, *J. Microsc.* **210**, 311 (2003).
- F. Kuschewski, H.-G. von Ribbeck, J. Döring, S. Winnerl, L. M. Eng, and S. C. Kehr, *Appl. Phys. Lett.* **108**, 113102 (2016).
- M. Specht, J. D. Pedarnig, W. M. Heckl, and T. W. Hänsch, *Phys. Rev. Lett.* **68**, 476 (1992).
- Y. Inoué and S. Kawata, *Opt. Lett.* **19**, 159 (1994).
- F. Zenhausern, M. P. O'Boyle, and H. K. Wickramasinghe, *Appl. Phys. Lett.* **65**, 1623 (1994).
- X. Chen, D. Hu, R. Mescall, G. You, D. N. Basov, Q. Dai, and M. Liu, *Adv. Mater.* **31**, 1804774 (2019).
- H.-T. Chen, R. Kersting, and G. C. Cho, *Appl. Phys. Lett.* **83**, 3009 (2003).
- A. J. Huber, F. Keilmann, J. Wittborn, J. Aizpurua, and R. Hillenbrand, *Nano Lett.* **8**, 3766 (2008).
- H.-G. von Ribbeck, M. Brehm, D. W. van der Weide, S. Winnerl, O. Drachenko, M. Helm, and F. Keilmann, *Opt. Express* **16**, 3430 (2008).
- R. Jacob, S. Winnerl, H. Schneider, M. Helm, M. T. Wenzel, H.-G. von Ribbeck, L. M. Eng, and S. C. Kehr, *Opt. Express* **18**, 26206 (2010).
- C. Liewald, S. Mastel, J. Hesler, A. J. Huber, R. Hillenbrand, and F. Keilmann, *Optica* **5**, 159 (2018).
- T. Taubner, F. Keilmann, and R. Hillenbrand, *Opt. Express* **13**, 8893 (2005).
- A. A. Govyadinov, S. Mastel, F. Golmar, A. Chuvilin, P. S. Carney, and R. Hillenbrand, *ACS Nano* **8**, 6911 (2014).
- K. Moon, H. Park, J. Kim, Y. Do, S. Lee, G. Lee, H. Kang, and H. Han, *Nano Lett.* **15**, 549 (2015).
- L. Jung, B. Hauer, P. Li, M. Bornhöft, J. Mayer, and T. Taubner, *Opt. Express* **24**, 4431 (2016).
- L. Wehmeier, D. Lang, Y. Liu, X. Zhang, S. Winnerl, L. M. Eng, and S. C. Kehr, *Phys. Rev. B* **100**, 035444 (2019).
- P. Hermet, M. Goffinet, J. Kreisel, and P. Ghosez, *Phys. Rev. B* **75**, 220102 (2007).
- T. Taubner, F. Keilmann, and R. Hillenbrand, *Nano Lett.* **4**, 1669 (2004).

- ³⁰S. C. Schneider, J. Seidel, S. Grafström, L. M. Eng, S. Winnerl, D. Stehr, and M. Helm, *Appl. Phys. Lett.* **90**, 143101 (2007).
- ³¹S. C. Kehr, M. Cebula, O. Mieth, T. Härtling, J. Seidel, S. Grafström, L. M. Eng, S. Winnerl, D. Stehr, and M. Helm, *Phys. Rev. Lett.* **100**, 256403 (2008).
- ³²S. Amarie and F. Keilmann, *Phys. Rev. B* **83**, 045404 (2011).
- ³³H. Wang, L. Wang, D. S. Jakob, and X. G. Xu, *Nat. Commun.* **9**, 2005 (2018).
- ³⁴R. Hillenbrand, T. Taubner, and F. Keilmann, *Nature* **418**, 159 (2002).
- ³⁵F. Keilmann and R. Hillenbrand, *Philos. Trans. R. Soc. London Ser. A* **362**, 787 (2004).
- ³⁶A. Huber, N. Ocelic, T. Taubner, and R. Hillenbrand, *Nano Lett.* **6**, 774 (2006).
- ³⁷A. J. Huber, A. Ziegler, T. Köck, and R. Hillenbrand, *Nat. Nanotechnol.* **4**, 153 (2009).
- ³⁸L. M. Zhang, G. O. Andreev, Z. Fei, A. S. McLeod, G. Dominguez, M. Thiemens, A. H. Castro-Neto, D. N. Basov, and M. M. Fogler, *Phys. Rev. B* **85**, 075419 (2012).
- ³⁹M. Lewin, C. Baeumer, F. Gunkel, A. Schwedt, F. Gaussmann, J. Wueppen, P. Meuffels, B. Jungbluth, J. Mayer, R. Dittmann, R. Waser, and T. Taubner, *Adv. Funct. Mater.* **28**, 1802834 (2018).
- ⁴⁰J. Döring, D. Lang, L. Wehmeier, F. Kuschewski, T. Nörenberg, S. C. Kehr, and L. M. Eng, *Nanoscale* **10**, 18074 (2018).
- ⁴¹D. Lang, J. Döring, T. Nörenberg, D. Butykai, I. Kézsmárki, H. Schneider, S. Winnerl, M. Helm, S. C. Kehr, and L. M. Eng, *Rev. Sci. Instrum.* **89**, 033702 (2018).
- ⁴²O. Khatib, H. A. Bechtel, M. C. Martin, M. B. Raschke, and G. L. Carr, *ACS Photonics* **5**, 2773 (2018).
- ⁴³D. J. Lahneman, T. J. Huffman, P. Xu, S. L. Wang, T. Grogan, and M. M. Qazilbash, *Opt. Express* **25**, 20421 (2017).
- ⁴⁴L. Cheng, D.-L. Wang, S.-Y. Dai, Y.-D. Yan, X.-D. Fan, L.-M. Wei, and C.-G. Zeng, *J. Infrared Millimeter Waves* **36**, 534 (2017).
- ⁴⁵M. C. Giordano, S. Mastel, C. Liewald, L. L. Columbo, M. Brambilla, L. Viti, A. Politano, K. Zhang, L. Li, A. G. Davies, E. H. Linfield, R. Hillenbrand, F. Keilmann, G. Scamarcio, and M. S. Vitiello, *Opt. Express* **26**, 18423 (2018).
- ⁴⁶A. Borak, *Science* **308**, 638 (2005).
- ⁴⁷N. A. Aghamiri, F. Huth, A. J. Huber, A. Fali, R. Hillenbrand, R. Hillenbrand, and Y. Abate, *Opt. Express* **27**, 24231 (2019).
- ⁴⁸S. C. Schneider, S. Grafström, and L. M. Eng, *Phys. Rev. B* **71**, 115418 (2005).
- ⁴⁹S. C. Kehr, Y. M. Liu, L. W. Martin, P. Yu, M. Gajek, S.-Y. Yang, C.-H. Yang, M. T. Wenzel, R. Jacob, H.-G. von Ribbeck, M. Helm, X. Zhang, L. M. Eng, and R. Ramesh, *Nat. Commun.* **2**, 249 (2011).
- ⁵⁰Only the phonon data of Lobo *et al.* obtained on a BFO single crystal was measured on a sample with similar high crystalline quality like that of our epitaxially grown thin films. Note that the thin-film phonon data given in Ref. 6 was measured at 10 K.
- ⁵¹J. A. Porto, P. Johansson, S. P. Apell, and T. López-Ríos, *Phys. Rev. B* **67**, 085409 (2003).
- ⁵²B. Knoll and F. Keilmann, *Nature* **399**, 134 (1999).
- ⁵³B. Knoll and F. Keilmann, *Opt. Commun.* **182**, 321 (2000).
- ⁵⁴G. Wurtz, R. Bachelot, and P. Royer, *Rev. Sci. Instrum.* **69**, 1735 (1998).
- ⁵⁵S. C. Kehr, J. Döring, M. Gensch, M. Helm, and L. M. Eng, *Synchrotron Radiat. News* **30**, 31 (2017).
- ⁵⁶J. M. Klopff, M. Helm, S. C. Kehr, U. Lehnert, P. Michell, A. Pashkin, H. Schneider, W. Seidel, S. Winnerl, and S. Zvyagin, in 2018 43rd International Conference on Infrared, Millimeter, and Terahertz Waves (IRMMW-THz) (2018), pp. 1–2.
- ⁵⁷H. Shima, H. Naganuma, and S. Okamura, “Optical properties of multiferroic BiFeO₃ films,” in *Materials Science-Advanced Topics* (IntechOpen, 2013), pp. 33–61.